Journal of Fluorescence
https://doi.org/10.1007/s10895-018-2267-7

ORIGINAL ARTICLE

Lipid Bilayer Interactions of Amyloidogenic N-Terminal Fragment of Apolipoprotein A-I Probed by Förster Resonance Energy Transfer and Molecular Dynamics Simulations

Galyna P. Gorbenko[1] · Valeriya Trusova[1] · Chiharu Mizuguchi[2] · Hiroyuki Saito[2]

Received: 27 May 2018 / Accepted: 10 July 2018

Abstract
The effects of one of the amyloidogenic mutations of apolipoprotein A-I (apoA-I), G26R, on the thermal stability, structural dynamics and lipid-associating properties of the 1–83 N-terminal fragment of apoA-I (A83) have been investigated using the Förster resonance energy transfer (FRET) and molecular dynamics (MD) simulation. The measurements of FRET between the tryptophan residues of the single Trp variants of A83 as donors and the membrane-incorporated fluorescent probe 4-dimethylaminochalcone as an acceptor provided evidence for a less depth of A83/G26R penetration into phosphatidylcholine (PC) bilayer compared to WT counterpart. The unfolding MD simulations showed that G26R mutation destabilizes the overall structure of A83, with individual alpha-helices differing in their thermal stability. The MD simulations performed at physiological temperature revealed that A83 and A83/G26R differ in their conformational behavior in an aqueous solution, PC and PC/Cholesterol bilayers. These findings may prove of importance for deeper understanding of the key determinants of apoA-I amyloidogenesis.

Keywords N-terminal fragment of apolipoprotein A-I · Amyloidogenic mutation G26R · Protein-lipid interactions · Förster resonance energy transfer · Molecular dynamics

Introduction

A fundamental propensity of polypeptide chain to one-dimensional crystallization into cross-beta-structured aggregates (amyloid fibrils) currently attracts tremendous research interest in view of a causative link between amyloid formation and a number of human disorders [1]. Among such disorders are acquired and familial amyloidoses of apolipoprotein A-I (apoA-I), a major protein component of high density lipoproteins (HDL) [2]. ApoA-I is a 243-residue polypeptide containing 11/22-residue repeats of amphipathic α-helices that form N-terminal (residues 1–187) and C-terminal helix bundles [3, 4]. ApoA-I plays an important role in HDL structure and function through stabilizing the HDL assemblies and modulating the pathways of reverse cholesterol transport when excess cholesterol is transferred from cell membranes of peripheral tissues to the liver for catabolism [5, 6]. In this process, apoA-I exchanges between lipid-bound (~95%) and lipid-poor/lipid-free (~5%) forms, thereby regulating lipid metabolism and exerting an antiatherogenic effect [7]. On the other hand, lower thermodynamic stability of the free protein compared to its lipid-associated counterpart results in the apoA-I misassembly associated with two types of human amyloidosis [8–10]. In the acquired amyloidosis fibrillar aggregates of wild type full-length apoA-I are observed in atherosclerotic plaques [8], while in familial systemic amyloidosis amyloid deposits consisting of N-terminal 80–100 residues are found in the peripheral nerves, heart, gastrointestinal tract, liver and kidney [9, 10]. The latter type of amyloidosis is caused by specific mutations of apoA-I that are supposed to destabilize the N-terminal helix bundle thus facilitating the proteolytic cleavage of the full-length protein.[11,12] To date, about 20

✉ Galyna P. Gorbenko
galyna.p.gorbenko@karazin.ua

[1] Department of Nuclear and Medical Physics, V.N. Karazin Kharkiv National University, 4 Svobody Sq, Kharkiv 61022, Ukraine

[2] Department of Biophysical Chemistry, Kyoto Pharmaceutical University, 5 Nakauchi-cho, Misasagi, Yamashina-ku, Kyoto 607-8414, Japan

Published online: 15 July 2018

amyloidogenic mutations of apoA-I have been identified and grouped into inside mutations, located in the N-terminus (residues 1–100), and outside mutations occurring within the region 154–178 [11–14]. Among the latter are, in particular, the point mutations G26R, E34K, W50R, L60R, L64P, F71Y and L75P that have been shown to exert diverse effects on the apoA-I structure and dynamics, producing the destabilization of the N-terminal helix bundle, solvent exposure of hydrophobic groups, decrease of the protein compactness and increase of its flexibility and susceptibility to proteases [15]. The sequence analysis of apoA-I revealed four segments with the highest aggregation propensity, so called "hot spots" encompassing the residues 14–22, 53–58, 69–72 and 227–232 [16]. It has been hypothesized that the local destabilization of these segments upon mutations initiates their conversion from the native α-helices to β-structure, with a parallel intermolecular β-zipper propagating from the N- to C-terminus and eventually leading to fibrillization of the full-length protein or its N-terminal fragment [16]. However, it still remains unclear to what extent all the above factors modulate the amyloidogenic properties of the apoA-I. Another important point that requires further elucidation concerns the role of lipids in the apoA-I misfolding and fibril formation. On the one hand, a lipid environment has been supposed to stabilize the α-helical conformation of apoA-I, preventing in such a way the amyloid assembly [15]. On the other hand, amyloidogenic mutations seem to compromise the stability of α-helices in the lipid-bound state thus facilitating fibril growth, as was recently demonstrated for the apoA-I 1–83 fragment with G26R substitution [17]. As a further step towards uncovering the precise mechanisms by which lipids can modulate the apoA-I fibril-forming ability, herein we explored the conformational dynamics and lipid-associating properties of the apoA-I 1–83 fragment (A83) and its amyloidogenic counterpart A83/G26R. Our goal was twofold: i) to characterize the structure of the protein-lipid complexes through measuring the efficiency of the Förster energy transfer (FRET) between the Trp residues W8 or W50 of single Trp variants of A83 as donors and the membrane fluorophore, 4-dimethylaminochalcone (DMC) as an acceptor; ii) to compare the conformational behavior of the WT and mutated proteins using the all-atom molecular dynamics simulations.

Materials and Methods

ApoA-I Proteins

The single tryptophan variants of the N-terminal 1–83 fragment of human apoA-I A83/W8, A83/W50, A83/G26R/W8, A83/G26R/W50 were expressed and purified as described earlier [18]. The cDNA encoding the N-terminal fragment 1–83 of apoA-I was obtained by PCR with full-length human apoA-I cDNA serving as a template. The required combinations of mutations were introduced using the QuikChange site-directed mutagenesis kit (Stratagene, La Jolla, CA). Since two extra amino acids, Gly and Ser, were attached at the amino terminus of the target apoA-I, the two residues preceding the normal apoA-I sequence are numbered −1 and −2. The apoA-I preparations were at least 95% pure as assessed by SDS-PAGE. In all experiments, the examined apoA-I variants were freshly dialyzed from 6 M guanidine hydrochloride solution into 10 mM Tris buffer (150 mM NaCl, 0.01% NaN_3, pH 7.4) before use.

Preparation of Lipid Vesicles

Egg yolk phosphatidylcholine (PC) and cholesterol (Chol) were purchased from Avanti Polar Lipids (Alabaster, AL). 4-dimethylaminochalcone (DMC) was from Signe (Latvia). Large unilamellar vesicles were prepared from PC and PC/Chol (30 mol% Chol) mixtures using extrusion technique. The thin lipid film was obtained by evaporation of lipid ethanol solutions and then hydrated with 1.2 ml of 10 mM Tris buffer, 150 mM NaCl, 0.01% NaN_3 to yield the final lipid concentration 5 mM. Subsequently, lipid suspension was extruded through a 50 nm pore size polycarbonate filter.

Fluorescence Measurements

Fluorescence measurements were performed with a LS-55 spectrofluorimeter (Perkin-Elmer Ltd., Beaconsfield, UK) using 10 mm path-length quartz cuvettes. The apoA-I Trp fluorescence was selectively excited at 296 nm. Excitation and emission band passes were set at 10 nm. The efficiency of the Forster resonance energy transfer between Trp as a donor and DMC as an acceptor was determined by measuring the decrease of the protein fluorescence upon increasing the DMC concentration. The protein-lipid mixtures containing the buffer (1.86 ml), 50 μM protein solution (40 μl) and 5 mM liposome suspension (100 μl) were incubated 1 h at 37 °C and then titrated with aliquots (10 μl) of DMC solution in ethanol (115 μM). The steady-state fluorescence anisotropies of Trp and DMC were measured at excitation / emission wavelengths 296/350 or 420/500 nm, respectively, with excitation and emission band passes set at 15 nm (Trp) or 5 nm (DMC).

Molecular Dynamics Simulations

The molecular dynamics simulations were performed with GROMACS software (version 5.1) using the CHARM M36m force field [19]. The calculations were done at a temperature 310 K and a pressure 1 bar. The starting A83 structure for the thermal unfolding simulations was obtained from the crystal structure of C-terminally truncated apoA-I (PDB entry 3R2P). The web-based graphical interface CHARMM-GUI

was used to introduce the G26R mutation in the A83 sequence and prepare the input files for MD calculations [20]. The lipid bilayers were built from POPC and its mixture with cholesterol (30 mol%). The protein initial position relative to the lipid/water interface was predicted using the PPM server [21]. The protein-lipid complexes were solvated in the rectangular box $80 \times 80 \times 80$ A^3 with a minimum distance of 10 Å to the edges of the box. The TIP3P water model was used. To obtain a neutral total charge of the system six or five potassium counterions were added. The Particle Mesh Ewald algorithm was employed to treat the long-range electrostatic interactions [22]. The minimization and equilibration of the system were performed during 100 ps and 500 ps, respectively. The time step for MD simulations was 2 fs. The trajectories and coordinates were saved every 2 ps for further analysis. The whole time interval for MD calculations was 100 ns.

The analysis tools provided by GROMACS were used to calculate the root mean-square deviations (RMSD), root mean-square fluctuations (RMSF), radius of gyration (Rg) and solvent-accessible surface area (SASA) per residue. The clustering of the protein conformations was performed with the GROMACS tool gmx cluster using the gromos method based on the algorithm described by Daura et al. [23]. The cutoff was set as 0.3 nm. The evolution of the secondary structure was followed using the VMD Timeline tool and Tcl scripts.

Results and Discussion

Partition Model

The first step of the study was focused on quantifying the acceptor partitioning into lipid phase. To this end, DMC was titrated with the liposomes and the observed fluorescence intensity increase (ΔI) at the emission maximum was represented as a function of lipid concentration (Fig. 1a). In terms of the partition model [24] ΔI can be written as:

$$\Delta I = I_L - I_W = \frac{K_p V_L (I_{\max} - I_W)}{1 + K_p V_L} = \frac{K_p V_L \Delta I_{\max}}{1 + K_p V_L} \quad (1)$$

where I_L is the fluorescence intensity observed in the liposome suspension at a certain lipid concentration; I_W is the probe fluorescence intensity in a buffer solution; $I_{\max}$is the limit fluorescence in a lipid environment; V_L is the volume of a lipid phase; K_p is the dye partition coefficient defined as:

$$K_p = \frac{N_L' V_W}{N_W' V_L} \quad (2)$$

here N_L', N_W' are the moles of the dye in the lipid and aqueous phases, respectively; V_W is the volume of the aqueous phase.

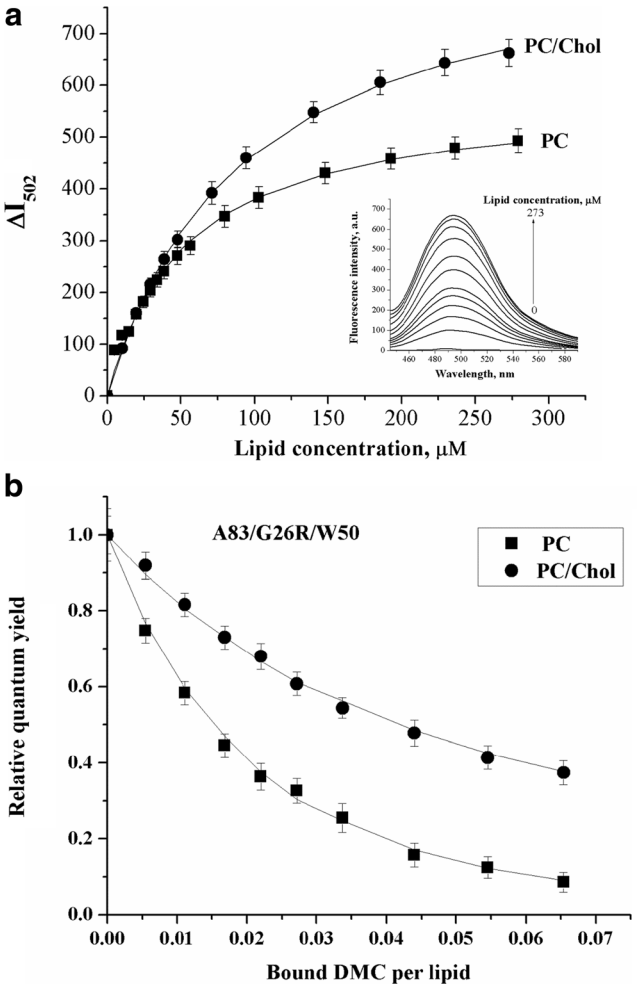

Fig. 1 **a** The isotherms of DMC binding to PC and PC/Chol liposomes. Probe concentration was 0.6 μM. Shown in inset are DMC emission spectra recorded at increasing concentration of PC/Chol liposomes. **b** FRET profiles measured for A83/G26R/W50 apoA-I variant. Protein and lipid concentrations were 2 and 50 μM, respectively. Solid lines represent theoretical curves calculated from Eqs. (1) to (23)

The volume of a lipid phase was calculated as:

$$V_L = N_A C_L \sum \nu_i f_i \quad (3)$$

where C_L is the molar lipid concentration, f_i is mole fraction of the *i-th* bilayer constituent, ν_i is its molecular volume taken as 1.58 nm^3 (PC) and 0.74 nm^3 (Chol). For cholesterol-containing systems the condensing effect of this lipid was taken into account, so that the above ν value was reduced by the factor 1.3. Under the employed experimental conditions ($C_L < 1$ mM) the V_L value is much less than total volume of the system ($V_t = 1$ dm^3), so that $V_W \approx V_t$. The approximation of the experimental dependencies $\Delta I(C_L)$ by the Eqs. (1)–(3) yielded the dye partition coefficients for PC and PC/Chol liposomes, $(2 \pm 0.5) \times 10^4$ and $(1.2 \pm 0.3) \times 10^4$, respectively. These partition coefficients were used to calculate the amount of the membrane-bound dye required for the quantitative analysis of the FRET data.

FRET Model

The results of FRET measurements have been quantitatively interpreted in terms of the model of energy transfer on a surface initially formulated by Fung & Stryer [25] and extended in our previous studies to allow for the distance dependence of orientation factor in two-dimensional systems [26]. Assuming that donors and acceptors are randomly distributed in different planes separated by a distance d_a, the efficiency of energy transfer is given by:

$$E = 1 - \int_0^\infty \exp(-\lambda)\exp\left(-C_a^s S(\lambda)\right)d\lambda \tag{4}$$

$$S(\lambda) = \int_{d_a}^\infty \left[1 - \exp\left(-\lambda\left(\frac{R_o}{R}\right)^6\right)\right] 2\pi R dR \tag{5}$$

where $\lambda = t/\tau_d$, τ_d is the lifetime of excited donor in the absence of acceptor, R_o is the Förster radius, C_a^s is the concentration of acceptors per unit area related to the molar concentrations of the bound probe (Z_b) and lipid (C_L):

$$C_a^s = \frac{Z_b}{C_L\left(f_{PC}S_{PC} + f_{Chol}S_{Chol}\right)} \tag{6}$$

here f, S are the mole fractions and mean areas per PC or Chol molecules taken as S_{PC} = 0.65 nm^2, S_{Chol} = 0.39 nm^2. The Förster radius is known to depend on the donor quantum yield (Q_D) and the overlap between the donor emission ($F_D(\lambda)$) and acceptor absorption ($\varepsilon_A(\lambda)$) spectra:

$$\begin{aligned} R_o &= 979\left(\kappa^2 n_r^{-4} Q_D J\right)^{1/6}; \\ J &= \frac{\int_0^\infty F_D(\lambda)\varepsilon_A(\lambda)\lambda^4 d\lambda}{\int_0^\infty F_D(\lambda)d\lambda} \end{aligned} \tag{7}$$

where n_r is the refractive index of the medium (n_r = 1.37). The quantum yields of the apoA-I variants estimated with tryptophan solution in water (Q = 0.14) as a standard, were found to lie in the range 0.02–0.03. The orientation factor (κ^2) is defined as:

$$\kappa^2 = \left(\sin\theta_D \sin\theta_A \cos\varphi - 2\cos\theta_D \cos\theta_A\right)^2 \tag{8}$$

where θ_D and θ_A are the angles between the donor emission (***D***) or acceptor absorption (***A***) transition moments and the vector ***R*** joining the donor and acceptor, φ is the dihedral angle between the planes (***D***, ***R***) and (***A***, ***R***).

The applicability of Eq. (8) is limited to the case where the vectors ***D*** and ***A*** do not undergo any reorientation during the transfer time. Alternatively, the Förster radius should be calculated using the dynamic average value of orientation factor ($\langle\kappa^2\rangle$). If the donor emission and acceptor absorption transition moments are symmetrically distributed within the cones about certain axes $\boldsymbol{D_x}$ and $\boldsymbol{A_x}$, $\langle\kappa^2\rangle$ is given by:

$$\begin{aligned} \langle\kappa^2\rangle = {} & \left(\sin\Theta_D \sin\Theta_A \cos\Phi - 2\cos\Theta_D \cos\Theta_A\right)^2 \langle d_D^x\rangle\langle d_A^x\rangle \\ & + 1/3\left(1 - \langle d_D^x\rangle\right) + 1/3\left(1 - \langle d_A^x\rangle\right) + \\ & + \cos^2\Theta_D \langle d_D^x\rangle\left(1 - \langle d_A^x\rangle\right) + \cos^2\Theta_A \langle d_A^x\rangle\left(1 - \langle d_D^x\rangle\right) \end{aligned} \tag{9}$$

where Θ_D and Θ_A are the angles made by the axes $\boldsymbol{D_x}$ and $\boldsymbol{A_x}$ with the vector ***R***, Φ is the angle between the planes containing the cone axes and the vector ***R***, $\langle d_D^x\rangle$ and $\langle d_A^x\rangle$ are so-called axial depolarization factors:

$$\left\langle d_{D,A}^x \right\rangle = 3/2\left\langle \cos^2\psi_{D,A}\right\rangle - 1/2 \tag{10}$$

where $\psi_{D,A}$ are the cone half-angles. These factors are related to the steady-state (r) and fundamental (r_0) anisotropies of donor and acceptor [27]:

$$d_{D,A}^x = \pm\left(r_{D,A}/r_{0D,A}\right)^{1/2} \tag{11}$$

The measured steady-state fluorescence anisotropies were similar for PC and PC/Chol systems, varying in the limits 0.15–0.19 for Trp and 0.18–0.21 for DMC. The fundamental anisotropies of Trp and DMC were taken as 0.3 and 0.39, respectively.

When the donor and acceptor planar arrays are located at different levels across the membrane the multiple donor-acceptor pairs are involved in energy transfer, so that orientation factor appears to be a function of the donor-acceptor separation (R). Particularly, for the most probable membrane orientation of $\boldsymbol{D_x}$ and $\boldsymbol{A_x}$, parallel to the bilayer normal, the angles Θ_D and Θ_A made by $\boldsymbol{D_x}$ and $\boldsymbol{A_x}$ with ***R*** are equal and depend on the donor-acceptor distance ($\Theta_A = \Theta_D = \theta$, $\theta = f(R)$). Under these circumstances Eq. (9) can be rewritten in the form:

$$\begin{aligned} \langle\kappa^2(\theta)\rangle = {} & \langle d_D^x\rangle\langle d_A^x\rangle\left(3\cos^2\theta - 1\right)^2 + 1/3\left(1 - \langle d_D^x\rangle\right) + \\ & + 1/3\left(1 - \langle d_A^x\rangle\right) + \cos^2\theta\left(\langle d_D^x\rangle - 2\langle d_D^x\rangle\langle d_A^x\rangle + \langle d_A^x\rangle\right) \end{aligned} \tag{12}$$

where $\cos^2\theta = (d_a/R)^2$. Next, by representing the Förster radius as $R_o = \left[\kappa^2(R)\right]^{1/6} \cdot R_o^r$ one obtains:

$$\begin{aligned} S(t) &= \int_{d_a}^\infty \left[1 - \exp\left(-\lambda\kappa^2(R)\left(\frac{R_o^r}{R}\right)^6\right)\right] 2\pi R dR; \\ R_o^r &= 979\left(n_r^{-4} Q_D J\right)^{1/6} \end{aligned} \tag{13}$$

In analyzing the FRET data presented here we considered the lipid-protein systems as containing one donor plane located at a distance d_c from the membrane center and two acceptor planes separated by a distance d_t. Given that for the outer acceptor plane $d_a = |d_c - 0.5d_t|$ while for the inner plane $d_a = d_c + 0.5d_t$, the following relationships hold:

$$S_1(\lambda) = \int_{|d_c - 0.5d_t|}^\infty \left[1 - \exp\left(-\lambda\kappa_1^2(R)\left(\frac{R_o^r}{R}\right)^6\right)\right] 2\pi R dR \tag{14}$$

$$S_2(\lambda) = \int_{d_c+0.5d_t}^{\infty} \left[1-\exp\left(-\lambda\kappa_2^2(R)\left(\frac{R_o^r}{R}\right)^6\right)\right] 2\pi R dR \quad (15)$$

$$\kappa_{1,2}^2(R) = \langle d_D^x\rangle\langle d_A^x\rangle\left(3\left(\frac{d_c\mp 0.5d_t}{R}\right)^2-1\right) + \frac{1-\langle d_D^x\rangle}{3}+\frac{1-\langle d_A^x\rangle}{3}+ + \left(\frac{d_c\mp 0.5d_t}{R}\right)^2\left(\langle d_D^x\rangle-2\langle d_D^x\rangle\langle d_A^x\rangle+\langle d_A^x\rangle\right) \quad (16)$$

$$E = 1-Q_r = 1-\int_0^{\infty}\exp(-\lambda) \exp\left[-C_a^s(S_1(\lambda)+S_2(\lambda))\right]d\lambda \quad (17)$$

where Q_r is the relative quantum yield; S_2 and S_2 are the quenching contributions describing the energy transfer to the outer and inner acceptor planes, respectively. The relationships (14)–(17) are valid when the donor and acceptor transition moments are distributed about the axes $\boldsymbol{D_x}$ and $\boldsymbol{A_x}$ parallel to the bilayer normal $\boldsymbol{N}$. If this is not the case, additional depolarization factors accounting for the deviations of $\boldsymbol{D_x}$ and $\boldsymbol{A_x}$ from $\boldsymbol{N}$ should be introduced: $d_{D,A}^a = \frac{3}{2}\cos^2\alpha_{D,A}-\frac{3}{2}$, where $\alpha_{D,\,A}$ are the angles made by $\boldsymbol{D_x}$ and $\boldsymbol{A_x}$ with $\boldsymbol{N}$. By applying the Soleillet's theorem stating the multiplicativity of depolarization factors, Eq. (16) may be rewritten in a more general form:

$$\kappa_{1,2}^2(R) = d_D d_A\left(3\left(\frac{d_c\mp 0.5d_t}{R}\right)^2-1\right) + \frac{1-d_D}{3}+\frac{1-d_A}{3}+ + \left(\frac{d_c\mp 0.5d_t}{R}\right)^2(d_D-2d_D d_A+d_A) \quad (18)$$

where $d_{D,A} = \left\langle d_{D,A}^x\right\rangle d_{D,A}^a$.

In the above FRET model the spatial relationships between the donors and acceptors are defined by the parameters d_c and d_t, characterizing the distance between the donor plane and membrane center, and separation between the outer and inner acceptor planes, respectively. The former parameter was optimized while the latter was taken as 2.6 nm, allowing that DMC molecules are located at the level of glycerol backbone and upper acyl chain carbons.

Since only the membrane-bound protein molecules are involved in FRET, the measured fluorescence intensity (F^m) can be represented as a sum of variable term (depending on acceptor concentration) and virtually invariant term (experiencing only slight changes due to the sample dilution and inner filter effect). In general, for the *i-th* point of fluorescence titration of the protein-lipid mixture by the probe one can write:

$$F_i^m = F_i^b + F_i^f + F_i^L \quad (19)$$

where superscripts b and f refer to the bound and free protein, respectively; F_i^L is the contribution of light scattering. Next, the difference $F_i^{corrL} = \left(F_i^m-F_i^L\right)K_{IFE}$ (K_{IFE} is the coefficient correcting for the inner filter effects) can be represented as:

$$F_i^{corrL} = F_i^b + F_i^f = P_i\left[f_{bi}a_{bi}-(1-f_{bi})a_f\right] \quad (20)$$

here f_b is the molar fraction of the bound protein, a_b and a_f are the molar fluorescences of the bound and free protein, respectively. The protein fluorescence intensity measured in the presence of DMC was corrected for inner filter effect using the following coefficients [28]:

$$K_{IFE} = \frac{\left(1-10^{-A_o^{ex}}\right)\left(A_o^{ex}+A_a^{ex}\right)}{\left(1-10^{-\left(A_o^{ex}+A_a^{ex}\right)}\right)A_o^{ex}}\frac{\left(1-10^{-A_o^{em}}\right)\left(A_o^{em}+A_a^{em}\right)}{\left(1-10^{-\left(A_o^{em}+A_a^{em}\right)}\right)A_o^{em}} \quad (21)$$

where A_o^{ex}, A_o^{em} are the donor optical densities at the excitation and emission wavelengths in the absence of acceptor, A_a^{ex}, A_a^{em} are the acceptor optical densities at the excitation and emission wavelengths, respectively. In fact, the relative quantum yield (Q_{ri}) is determined by the ratio of the molar fluorescence of bound protein at the *i-th* acceptor concentration (a_{bi}) to that observed at the initial titration point, in the absence of acceptor (a_{bo}):

$$Q_{ri} = \frac{a_{bi}}{a_{bo}} \quad (22)$$

Rearranging Eq. (20) one obtains:

$$a_{bi} = \frac{F_i^{corrL}-(1-f_{bi})a_f P_i}{f_{bi}P_i}; \quad a_{bo} = \frac{F_o^{corrL}-a_f P_o}{f_{bo}P_o} \quad (23)$$

As follows from the above considerations, the measured FRET profiles depend on the fraction of bound protein. For this reason, the FRET model was combined with the partition model (Eqs. (1)–(3)) describing the protein-lipid binding in terms of the partition coefficient K_{PL}. Based on the above formalism, the experimental FRET profiles have been quantitatively analyzed with simultaneous optimization of the structural parameter (Trp distance from the bilayer center, d_c) and the binding parameter (partition coefficient K_{PL}).

FRET Analysis

Figure 1b illustrates the typical FRET profiles observed for the model systems containing one of the examined apoA-I

variants and monolamellar liposomes from PC or PC mixture with 30 mol% cholesterol. It appeared that the variations in both the protein and lipid composition of the investigated systems affect the efficiency of energy transfer. To interpret the FRET results quantitatively, we employed the combined FRET-binding model which describes the FRET profiles in terms of the two main quantities – the structural parameter, Trp distance from the center of lipid bilayer, and the binding parameter, the partition coefficient characterizing the protein-lipid association. These parameters have been estimated through the fitting of the theoretical curves predicted by the above model (Eqs. (1)–(23)) to the experimental FRET profiles. The principal outcomes of the FRET data analysis are as follows. (1) In PC bilayer W8 and W50 are situated at the distances 1.5–2 nm from the bilayer center (Fig. 2a), with G26R mutation resulting in a more exposed location of the Trp residues. (2) The experimental finding that for all the examined apoA-I variants the energy transfer becomes markedly less efficient in the presence of cholesterol can be explained by a much shallower location of the proteins relative to the membrane surface with W8 and W50 residing in the aqueous phase, at the distances 3.2–3.9 nm from the bilayer midplane (Fig. 2a). (3) The partition coefficients (Fig. 2b), and, accordingly, the values of the fraction of bound protein are generally higher in the PC/Chol membranes compared to the neat PC bilayers. Notably, the above estimates of the Trp distance from the PC bilayer center agree with the previously reported data indicating that in the lipid-associated state A83/W8 and A83/W50 variants have emission maxima at lower wavelengths compared to their A83/G26R/W8 and A83/G26R/W50 analogs [17]. Furthermore, the observation that the fraction of bound protein is greater in PC/Chol bilayers supports the idea that cholesterol-induced increase of the phospholipid headgroup spacing favors the apoA-I binding to the membrane surface [29].

Thermal Unfolding MD Simulations

Next, to gain deeper understanding of the molecular factors underlying the effect of G26R mutation and lipids on the conformational behavior of N-terminal fragment of apoA-I, we performed the molecular dynamics simulations of A83 and A83/G26R variants in solution and lipid environment. The starting A83 structure was obtained from the crystal structure of C-terminally truncated apoA-I (PDB entry 3R2P) [4]. First, we explored the overall stability of A83 and A83/G26R through simulating their thermal unfolding at the temperatures 500 K and 400 K. The unfolding pathways of WT A83 and its mutant were compared using the parameters characterizing both the global and local protein structure, the root mean-square deviation (RMSD), gyration radius (R_g), solvent accessible surface area (SASA), the root mean-square fluctuations of the C-alpha atoms (RMSF) and the secondary structure

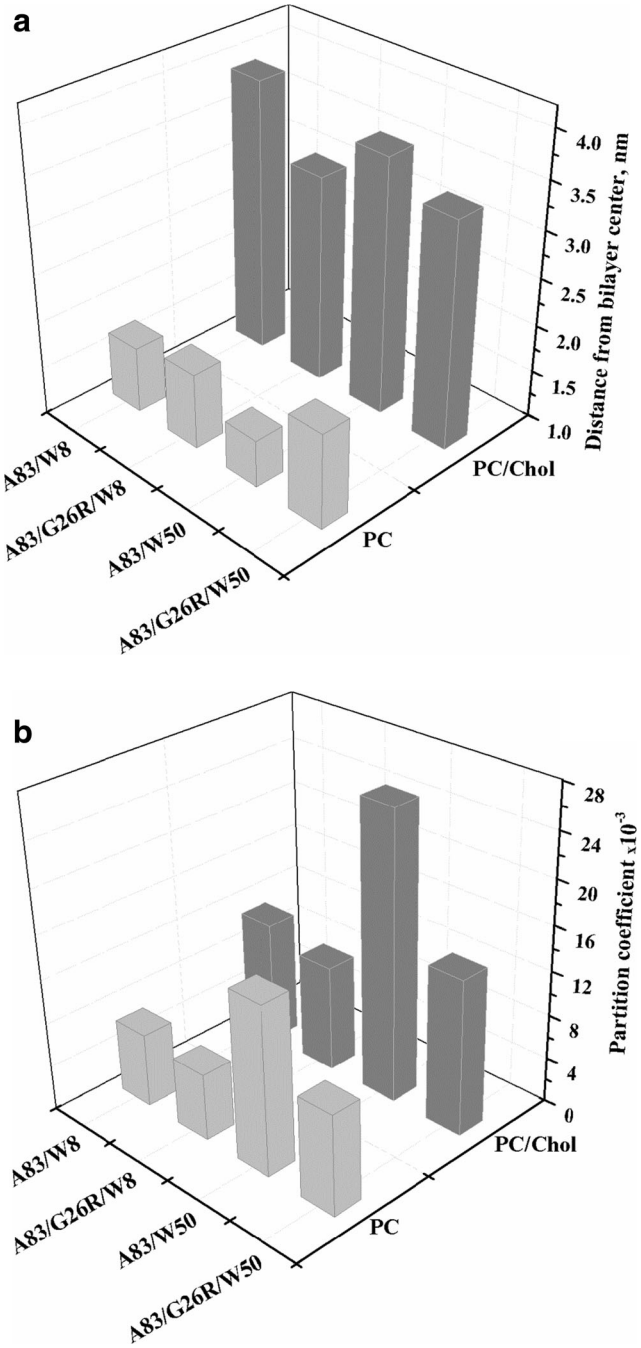

Fig. 2 **a** Distance between Trp residues 8 or 50 and lipid bilayer center. The error of distance estimation does not exceed 0.3 nm. **b** Partition coefficients characterizing the complexation of apoA-I variants with PC and PC/Chol bilayers

content. The RMSD trajectories for both A83 and A83/G26R increased similarly during the first 15 ns of simulation and then followed by the fluctuations around ~ 1.4 nm (400 K) or 2 nm (500 K). Analogously, no sustained differences between WT and mutated A83 were found in the time evolution of gyration radius, hydrophilic and hydrophobic SASA. On the contrary, analysis of the secondary structure profiles revealed that A83/G26R unfolds markedly faster than A83. As

illustrated in Fig. 3a, at 500 K the content of α-helices drops to about zero in ~5 ns for the mutant and in ~10 ns for the WT protein, while at 400 K the helicity reduced to ~40% for A83 and to ~35% for A83/G26R during ~30 ns and then fluctuates around these values (Fig. 3b). In the initial state A83 contains four α-helices encompassing the residues 7–35 (H1 37–42 (H2), 56–64 (H3) and 69–75 (H4). It appeared that these helices differ in their ability to convert into turns and coils during the unfolding process. Considering the helix as being completely unfolded if its helicity equals zero for at least 1 ns, we found that the unfolding time (t_u) of A83/G26R helices decreases in the row H1 (t_u ~ 4.5 ns) > H4 (t_u ~ 4.2 ns) > H2 (t_u ~ 2.7 ns) > H3 (t_u ~ 1.5 ns), while in A83 the helix stability follows the order H3 (t_u ~ 10.8 ns) > H4 (t_u ~ 10.5 ns) > H1 (t_u ~ 9.6 ns) > H2 (t_u ~ 8.3 ns) (Fig. 4). This finding indicates that G26R mutation differently affects

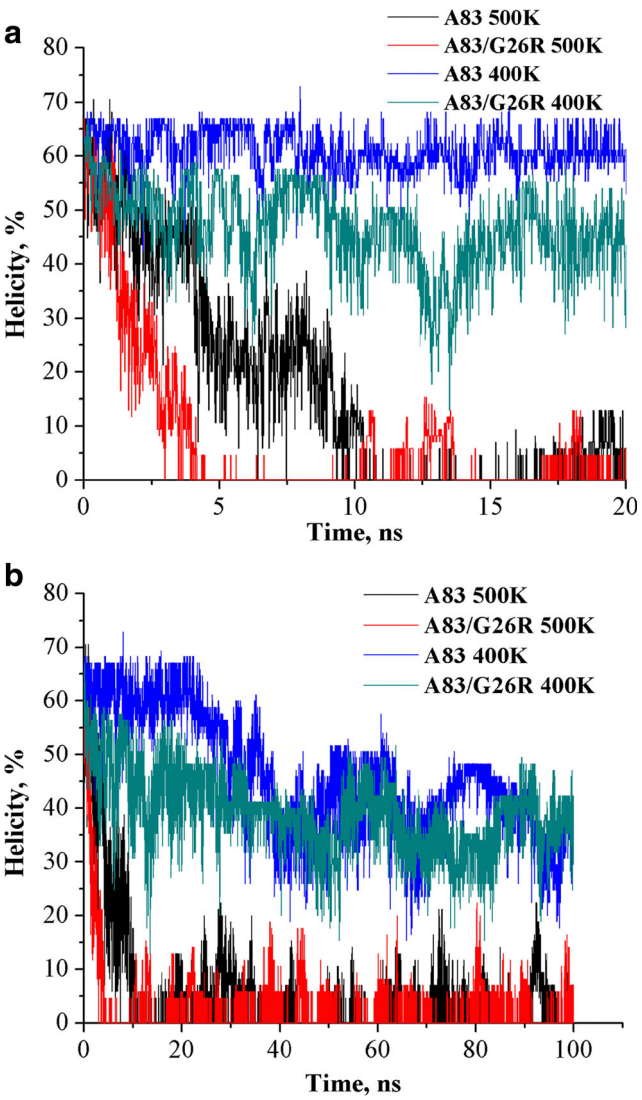

Fig. 3 **a** Plots of the helical content of A83 and A83/G26R as a function of time for 20 ns MD trajectory. **b** Helical content of A83 and A83/G26R as a function of time for 100 ns MD trajectory

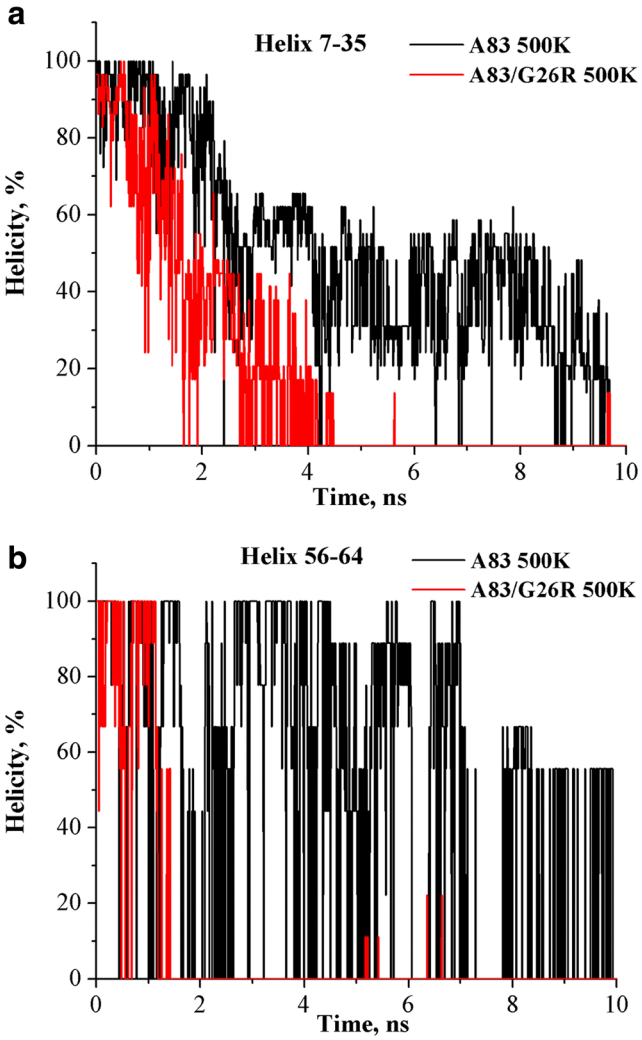

Fig. 4 Helicity of the individual α-helices of A83 and A83/G26R as a function of time: **a** Helix 7–35. **b** Helix 56–64

the stability of the individual α-helices, with the most pronounced destabilization (~ 7-fold decrease in t_u) being observed for the helix 56–64. Interestingly, this helix partially overlaps with the amyloid hot spot 53–58 predicted by the sequence-based algorithms [30]. Another observation noteworthy is that during the unfolding at 400 K the RMSF of the mutant are generally higher than that of WT protein (except the weakly fluctuating central fragment 32–42) with the most pronounced differences (>50%) being observed in the vicinity of the mutation site (residues 22–27) and in the regions 45–62 and 65–67, one of which covers the ApoA-I amyloid hot spot 53–58 (Fig. 5a). Notably, at 500 K the RMSF changes are markedly smaller in magnitude and seem to be less amenable to analysis because the temperatures higher than 400 K are supposed to influence the protein unfolding pathways through modifying the properties of water [31]. Remarkably, at both temperatures the largest increase in the average SASA per residue is observed for the mutated residue 26 (Fig. 5b).

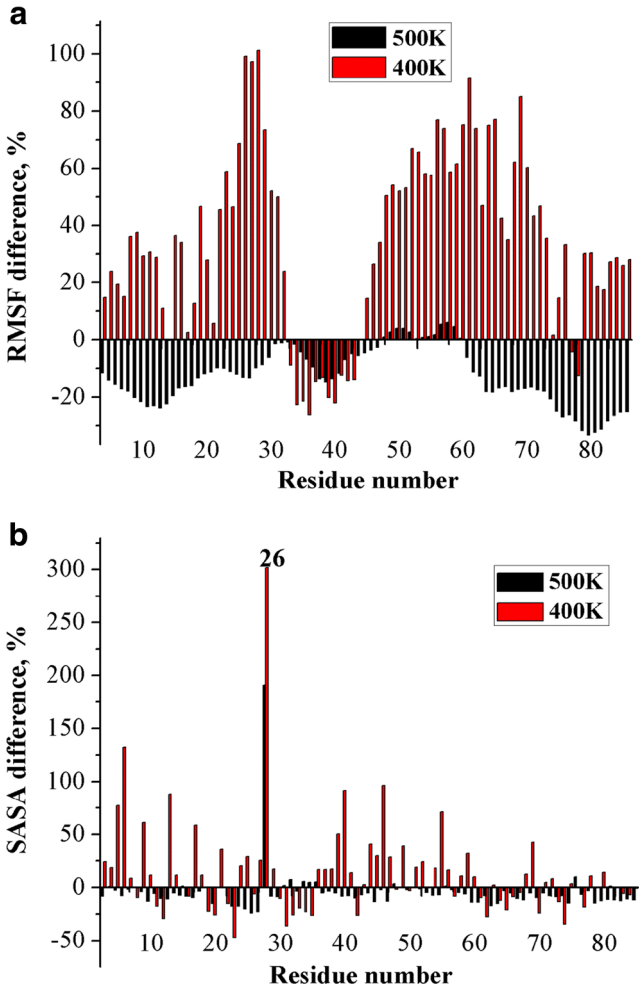

Fig. 5 **a** Percentage of difference between A83/G26R and A83 in RMSF calculated as $((RMSF_{Mut}/RMSF_{WT})) -1) \times 100$. **b** Percentage of difference between A83/G26R and A83 in average SASA per residue calculated as $((SASA_{Mut}/SASA_{WT})) -1) \times 100$

MD Simulations at Physiological Temperature

At the last step of the study, to elucidate the effect of lipids on the conformational properties of A83 and its G26R mutant, a series of MD simulations have been performed at physiological temperature, 310 K. In solution, at neutral pH, A83 and A83/G26R have predominantly a random coil conformation with the helical content ~15% [17]. This implies that the crystal structure of A83 whose helicity is ca. 65% is inappropriate for simulation of the protein dynamics in solution or lipid bilayer. To circumvent this problem, we employed the strategy involving the following principal steps: i) retrieving the ensemble of conformers with average helicity close to the experimental value 15% from the 500 K unfolding trajectory; ii) clustering the 500 K ensemble conformations into groups based on the RMSD values; iii) MD simulation of the 500 K cluster representative structures at 310 K; iv) clustering the conformers generated during the 310 K MD simulation and obtaining the 310 K ensemble from the representative structures of each cluster; v) analysis of the 310 K ensemble using the PPM2 method which allows to determine the protein spatial position relative to lipid-water interface [32] and calculate the frequency of the residue insertion into nonpolar bilayer region; vi) selection of the conformers anchored to the membrane in the most frequently occurred way; vi) MD simulation of the selected A83 and A83/G26R conformers in solution and lipid bilayer at 310 K. As shown in Fig. 6a, the G26R mutation modifies the mode of protein-lipid interactions. In the A83-PC system the residues most frequently penetrating the hydrophobic region of PC bilayer (with the frequency >20%) follow the order: L14 ~ L82 > R83 > T16 > W50 > A15, while for A83/G26R the analogous row is F57 > L82 > L38 > R83 ~ W50. The

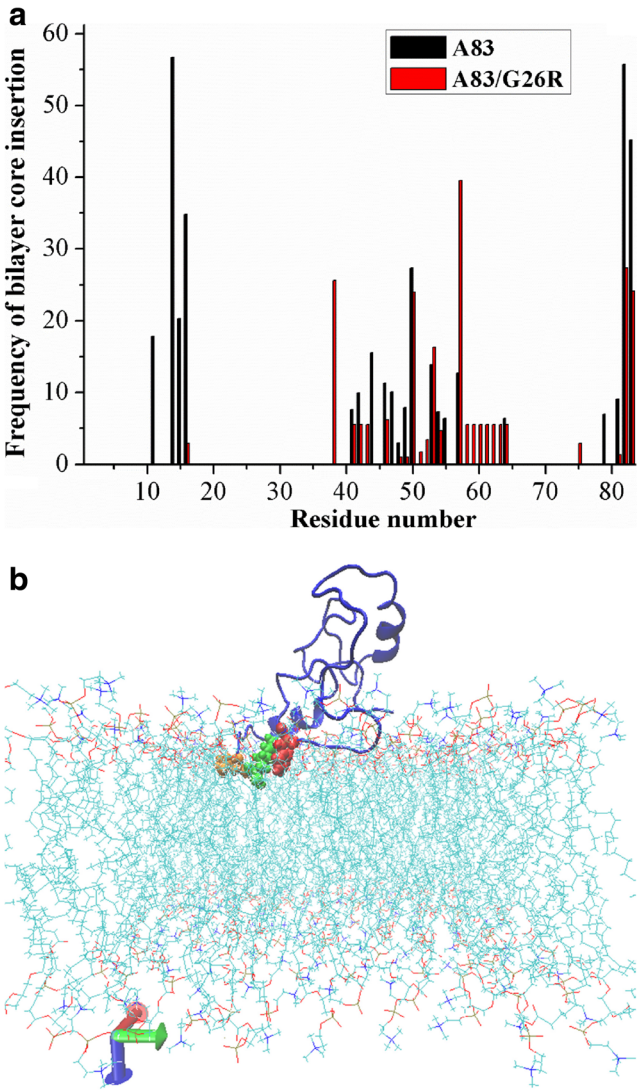

Fig. 6 **a** The frequency of residue penetration in the hydrophobic region of PC bilayer. **b** Disposition of A83 conformer used in MD simulation at 310 K with respect to the membrane surface. The residues penetrating into nonpolar bilayer region are marked in red (F57), orange (L82) and green (R83). The α-helices encompass the residues 27–34 and 67–72

similarity between WT and mutated proteins lies in the involvement of L82, R83 and W50 in the membrane anchoring, whereas the main differences concern the absence of any penetration of V11, L14, A15 and T16 into the membrane core, and much more pronounced bilayer insertion of L38 and F57 in the A83/G26R-lipid complexes. Importantly, the PPM prediction that W50 is a membrane-embedded residue is in harmony with the FRET results presented here and experimentally observed short-wavelength shift of the emission maximum of W50 apoA-I variants upon lipid binding [17]. In the following, to characterize the lipid-associating behavior of A83 and its G26R mutant in more detail, we performed the MD simulation of these proteins at 310 K. The conformers chosen for this purpose from the 310 K conformational ensemble attach to the lipid bilayer in such a manner that F57, L82 and R83 reside at the level of initial acyl chain carbons, as illustrated in Fig. 6b. The analysis of 100 ns MD trajectories revealed several key differences between the A83 and A83/G26R. (1) The protein helicity averaged over all trajectory increases upon membrane binding, with the magnitude of this effect being markedly higher in A83-PC system (~27%) compared to A83/G26R-PC system (~5%). This finding agrees with the CD data indicating that in the lipid-bound state apoA-I variants have higher content of α-helices compared to the free state [17]. In the PC/Chol bilayer lipid-induced helicity increase was comparable for A83 (~13%) and A83/G26R (~15%). (2) In the PC bilayer the mutant is generally less flexible than its WT counterpart, except the central region 34–39 and terminal region 79–83 where $RMSF_{Mut} > RMSF_{WT}$ (Fig. 7a), while in the PC/Chol bilayer the prevailing tendency is the higher fluctuations of the mutated protein (Fig. 7b). Interestingly, in a lipid-bound state the regions of the largest difference in RMSF (>30%) fully or partly cover the amyloid hot spots 14–22, 53–58 and 69–72. In water, the regions of the highest fluctuations cover the fragments 12–17, 25–26, 81–83 ($RMSF_{Mut} < RMSF_{WT}$) and 19–22, 32–38 ($RMSF_{Mut} > RMSF_{WT}$). (3) The greatest SASA per residue changes (more than 2-fold increase in the mutant compared to WT) were observed for the residues 3, 26, 36, 38, 39 (PC) and 4, 26, 30, 64, 65 (PC/Chol), as seen in Fig. 8. Remarkably, in the PC/Chol bilayer the mutated residue 26 shows markedly larger SASA increase (~9 times) compared to PC bilayer (~2.5 times). Taken together, the RMSF and SASA per residue changes are consistent with the above FRET data suggesting that in the presence of Chol A83 and its mutant tend to adopt a more superficial membrane location.

Finally, it should be noted that direct comparison between the MD results and FRET data presented here cannot be made because the simulation was performed only for a particular structure from the conformational ensemble, while the structural parameters derived from FRET represent the average over all membrane-bound conformers. Nevertheless, the main tendencies such as i) a more exposed bilayer location of W8 and W50 in A83/G26R-PC system compared to A83-PC system and ii) a shallower position of the A83 variants in PC/Chol bilayer relative to the neat PC bilayer are well reproduced in the MD simulations.

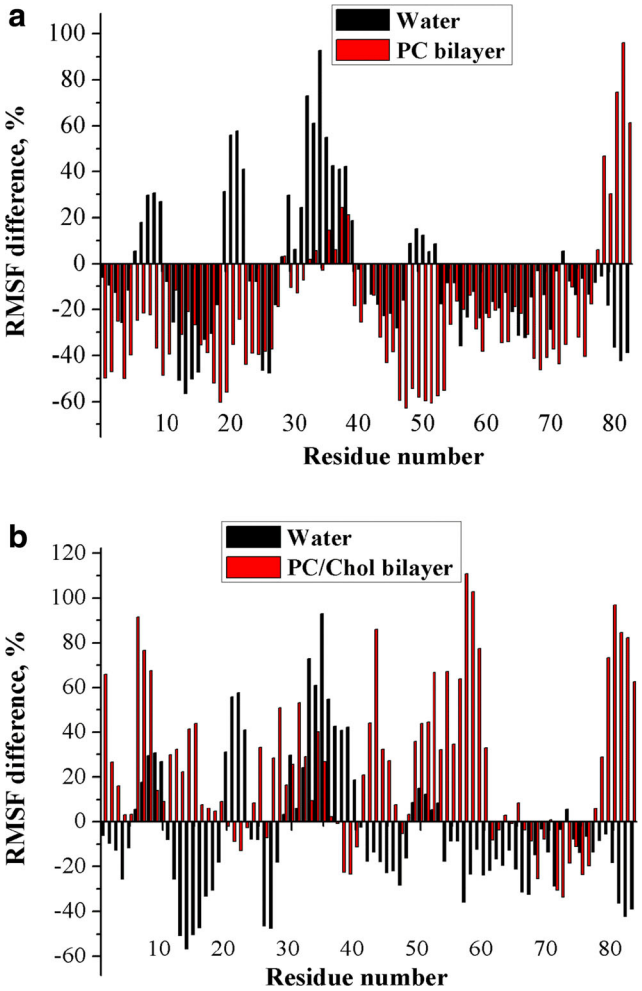

Fig. 7 Percentage of difference between A83/G26R and A83 in RMSF calculated from the results of 310 K MD simulation as $((RMSF_{Mut}/RMSF_{WT}) - 1) \times 100$ for PC (**a**) and PC/Chol (**b**) bilayers

Conclusions

Cumulatively, the present study revealed the diverse effects of the amyloidogenic mutation G26R on the structure, dynamics and lipid-associating properties of the 1–83 N-terminal fragment of apoA-I:

(i) destabilization of the overall A83 structure, with the lowest stability being displayed by the helix 56–64;

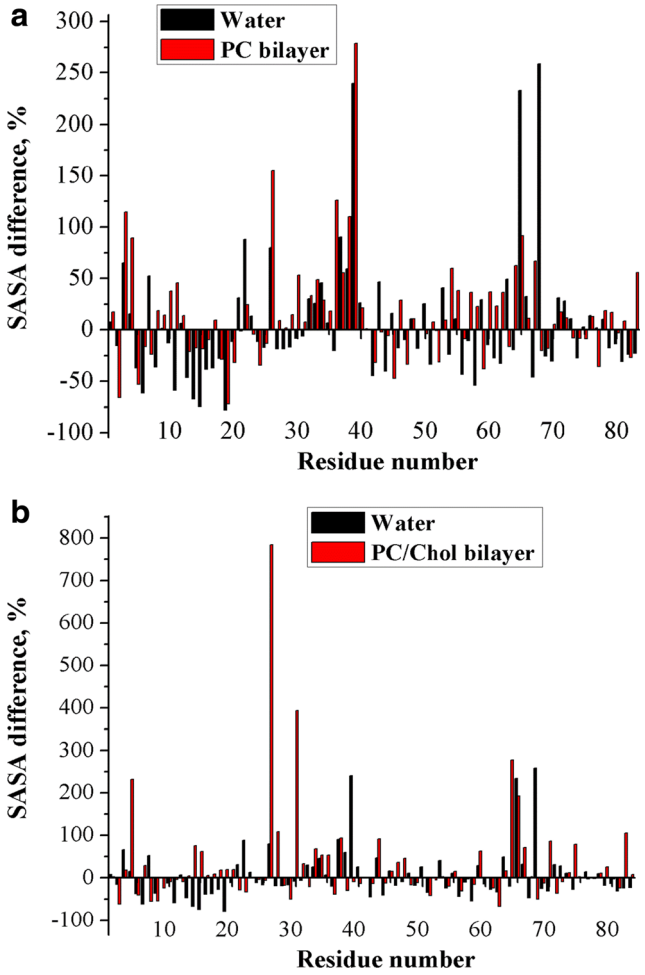

Fig. 8 Percentage of difference between A83/G26R and A83 in SASA calculated from the results of 310 K MD simulation as (($SASA_{Mut}$/$SASA_{WT}$) -1) × 100 for PC (**a**) and PC/Chol (**b**) bilayers

(ii) change of the protein location within the PC bilayer to a shallower position;
(iii) modification of the A83 membrane binding motif;
(iv) reduction of the magnitude of the protein helicity increase in the PC bilayer;
(v) alterations in the conformational dynamics of A83 both in free and lipid-bound states;
(vi) modulating influence of cholesterol on the bilayer location and conformational behavior of the WT and mutated A83.

These findings may prove essential for clarifying the subtle mechanisms of apoA-I amyloidogenesis and development of effective anti-amyloid strategies.

Acknowledgements This work was partly supported by the grants No 0116 U000937 and No 0117U004966 for Young Scientists from the Ministry of Education Science and of Ukraine (V.T.), JSPS KAKENHI Grant Number JP17H03979 (H.S.) and the Hyogo Science and Technology Association (H.S.).

Compliance with Ethical Standards

Conflict of Interest The authors declare that there is no conflict of interest associated with this study.

References

1. Dobson CM (2017) The amyloid phenomenon and its links with human disease. Cold Spring Harb Perspect Biol 9:a023648. https://doi.org/10.1101/cshperspect.a023648
2. Rosenson RS, Brewer HB Jr, Davidson WS, Fayad ZA, Fuster V, Goldstein J, Hellerstein M, Jiang X, Phillips MC, Rader DJ, Remaley AT, Rothblat GH, Tall AR, Yvan-Charvet L (2012) Cholesterol efflux and atheroprotection: advancing the concept of reverse cholesterol transport. Circulation 125:1905–1919. https://doi.org/10.1161/CIRCULATIONAHA.111.066589
3. Saito H, Dhanasekaran P, Nguyen D, Holvoet P, Lund-Katz S, Phillips MC (2003) Domain structure and lipid interaction in human apolipoproteins A-I and E, a general model. J Biol Chem 278:23227–23232. https://doi.org/10.1074/jbc.M303365200
4. Mei X, Atkinson D (2011) Crystal structure of C-terminal truncated apolipoprotein A-I reveals the assembly of high density lipoprotein (HDL) by dimerization. J Biol Chem 286:38570–38582. https://doi.org/10.1074/jbc.M111.260422
5. Rader DJ, Alexander ET, Weibel GL, Billheimer J, Rothblat GH (2009) The role of reverse cholesterol transport in animals and humans and relationship to atherosclerosis. J Lipid Res 50:S189–S194. https://doi.org/10.1194/jlr.R800088-JLR200
6. Phillips MC (2014) Molecular mechanisms of cellular cholesterol efflux. J Biol Chem 289:24020–24029. https://doi.org/10.1074/jbc.R114.583658
7. Pastore L, Belalcazar LM, Oka K, Cela R, Lee B, Chan L, Beaudet AL (2004) Helper dependent adenoviral vector-mediated long-term expression of human apolipoprotein A-I reduces atherosclerosis in apo E-deficient mice. Gene 327:153–160. https://doi.org/10.1016/j.gene.2003.11.024
8. Rocken C, Tautenhahn J, Buhling F, Sachwitz D, Vockler S, Goette A, Burger T (2006) Prevalence and pathology of amyloid in atherosclerotic arteries. Arterioscler Thromb Vasc Biol 26:676–677. https://doi.org/10.1161/01.ATV.0000201930.10103.be
9. Gursky O, Mei X, Atkinson D (2012) The crystal structure of the Cterminal truncated apolipoprotein A-I sheds new light on amyloid formation by the N-terminal fragment. Biochemistry 51:10–18. https://doi.org/10.1021/bi2017014
10. Rowczenio D, Dogan A, Theis JD, Vrana JA, Lachmann Ashutosh HJ, Wechalekar D, Gilbertson JA, Hunt T, Gibbs SD, Sattianayagam PT, Pinney JH, Hawkins PN, Gillmore JD (2011) Amyloidogenicity and clinical phenotype associated with five novel mutations in apolipoprotein A-I. Am J Pathol 179:1978–1987. https://doi.org/10.1016/j.ajpath.2011.06.024
11. Andreola A, Bellotti V, Giorgetti S, Mangione P, Obici L, Stoppini M, Torres J, Monzani E, Merlini G, Sunde M (2003) Conformational switching and fibrillogenesis in the amyloidogenic fragment of apolipoprotein A-I. J Biol Chem 278:2444–2451. https://doi.org/10.1074/jbc.M204801200
12. Obici L, Franceschini G, Calabresi L, Giorgetti S, Stoppini M, Merlini G, Bellotti V (2006) Structure, function and amyloidogenic propensity of apolipoprotein A-I. Amyloid 13:191–205. https://doi.org/10.1080/13506120600960288
13. Eriksson M, Schönland S, Yumlu S, Hegenbart U, von Hutten H, Gioeva Z, Lohse P, Büttner J, Schmidt H, Röcken C (2009) Hereditary apolipoprotein AI-associated amyloidosis in surgical pathology specimens: identification of three novel mutations in the

APOA1 gene. J Mol Diagn 11:257–262. https://doi.org/10.2353/jmoldx.2009.080161
14. Raimondi S, Guglielmi F, Giorgetti S, Di Gaetano S, Arciello A, Monti DM, Relini A, Nichino D, Doglia SM, Natalello A, Pucci P, Mangione P, Obici L, Merlini G, Stoppini M, Robustelli P, Tartaglia GG, Vendruscolo M, Dobson CM, Piccoli R, Bellotti V (2011) Effects of the known pathogenic mutations on the aggregation pathway of the amyloidogenic peptide of apolipoprotein A-I. J Mol Biol 407:465–476. https://doi.org/10.1016/j.jmb.2011.01.044
15. Arciello A, Piccoli R, Monti DM (2016) Apolipoprotein A-I: the dual face of a protein. FEBS Lett 590:4171–4179. https://doi.org/10.1002/1873-3468.12468
16. Das M, Mei X, Jayaraman S, Atkinson D, Gursky O (2014) Amyloidogenic mutations in human apolipoprotein A-I are not necessarily destabilizing – a common mechanism of apolipoprotein A-I misfolding in familial amyloidosis and atherosclerosis. FEBS J 281:2525–2542. https://doi.org/10.1111/febs.12809
17. Mizuguchi C, Ogata F, Mikawa S, Tsuji K, Baba T, Shigenaga A, Shimanouchi T, Okuhira K, Otaka A, Saito H (2015) Amyloidogenic mutation promotes fibril formation of the N-terminal apolipoprotein A-I on lipid membranes. J Biol Chem 290:20947–20959. https://doi.org/10.1074/jbc.M115.664227
18. Adachi E, Nakajima H, Mizuguchi C, Dhanasekaran P, Kawashima H, Nagao K, Akaji K, Lund-Katz S, Phillips MC, Saito H (2013) Dual role of an N-terminal amyloidogenic mutation in apolipoprotein A-I: destabilization of helix bundle and enhancement of fibril formation. J Biol Chem 288:2848–2856. https://doi.org/10.1074/jbc.M112.428052
19. Huang J, MacKerell A (2013) CHARMM36 all-atom additive protein force field: validation based on comparison to NMR data. J Comput Chem 34:2135–2145. https://doi.org/10.1002/jcc.23354
20. Jo S, Lim J, Klauda J, Im W (2009) CHARMM-GUI membrane builder for mixed bilayers and its application to yeast membranes. Biophys J 97:50–58. https://doi.org/10.1016/j.bpj.2009.04.013
21. Lomize M, Pogozheva I, Joo H, Mosberg H, Lomize A (2012) OPM database and PPM web server: resources for positioning of proteins in membranes. Nucleic Acids Res 40:D370–D376. https://doi.org/10.1093/nar/gkr703
22. Darden T, York D, Pedersen L (1993) Particle mesh Ewald: an N log(N) method for Ewald sums in large systems. J Chem Phys 98:10089–10092. https://doi.org/10.1063/1.464397
23. Daura X, Gademann K, Jaun B, Seebach D, van Gunsteren W, Mark A (1999) When simulation meets experiment. Angew Chem Int Ed 38:236–240. https://doi.org/10.1002/(SICI)1521-3773(19990115)38:1/2<236::AID-ANIE236>3.0.CO;2-M
24. Santos NC, Prieto M, Castanho MA (2003) Quantifying molecular partition into model systems of biomembranes: an emphasis on optical spectroscopic methods. Biochim Biophys Acta 161:123–135. https://doi.org/10.1016/S0005-2736(03)00112-3
25. Fung BK, Stryer L (1978) Surface density determination in membranes by fluorescence energy transfer. Biochemistry 17:5241–5248. https://doi.org/10.1021/bi00617a025
26. Gorbenko G, Handa T, Saito H, Molotkovsky J, Tanaka M, Egashira M, Nakano M (2003) Effect of cholesterol on bilayer location of the class a peptide ac-18A-NH2 as revealed by fluorescence resonance energy transfer. Eur Biophys J 32:703–709. https://doi.org/10.1007/s00249-003-0333-8
27. Dale R, Eisinger J, Blumberg W (1979) The orientational freedom of molecular probes. The orientation factor in intramolecular energy transfer. Biophys J 26:161–194. https://doi.org/10.1016/S0006-3495(79)85243-1
28. Bulychev AA, Verchoturov VN, Gulaev BA (1988) Current methods of biophysical studies. Vyschaya shkola, Moscow
29. Saito H, Miyako Y, Handa T, Miyajima K (1997) Effect of cholesterol on apolipoprotein A-I binding to lipid bilayers and emulsions. J Lipid Res 38:287–294
30. Das M, Gursky O (2015) Amyloid-forming properties of human apolipoproteins: sequence analyses and structural insights. Adv Exp Med Biol 855:175–211. https://doi.org/10.1007/978-3-319-17344-3_8
31. Walser R, Mark AE, van Gunsteren WF (2000) On the temperature and pressure dependence of a range of properties of a type of water model commonly used in high-temperature protein unfolding simulations. Biophys J 78:2752–2760. https://doi.org/10.1016/S0006-3495(00)76820-2
32. Lomize AL, Pogozheva ID, Mosberg HI (2011) Anisotropic solvent model of the lipid bilayer. 2. Energetics of insertion of small molecules, peptides, and proteins in membranes. J Chem Inf Model 51:930–946. https://doi.org/10.1021/ci200020k